Nanoscale

PAPER

View Article Online
View Journal

Cite this: DOI: 10.1039/d5nr04675k

Enhancing oxygen reduction reaction activity in ZIF-derived catalysts through thermal oxidation-induced micropore enlargement

Yu Joong Kim,†[a] Ki Hwan Koh,†[b] Hyeong Jun Kim,[a] Hyeonhoo Lee,[a] Sima Umrao,[a] Youn Jeong Jang *[c] and Tae Hee Han *[a,d]

Non-precious metal-based catalysts derived from metal–organic frameworks (MOFs), particularly zeolitic imidazolate frameworks (ZIFs), have gained attention as promising electrocatalysts for enhancing the oxygen reduction reaction (ORR) efficiency in energy conversion systems. However, the intrinsic microporous structure of ZIF-derived catalysts can hinder the mass transport of reactants to the active sites, thereby reducing the ORR mass activity (MA). In this paper, we present a novel strategy for improving the MA of ZIF-derived catalysts, which is an essential advancement in renewable energy storage and conversion technologies. While direct carbonization of ZIF precursors typically preserves this microporosity, limiting performance, we present a novel strategy to overcome this by employing a controlled thermal oxidation pre-treatment on Zn,Co-ZIF precursors. This pre-treatment introduces oxygen species and lattice strain into the framework, which act as *in situ* etching agents during subsequent pyrolysis, effectively converting micropores into mesopores. The resulting optimized catalyst (Co/N–C_3) exhibited a significant increase in mesopore volume and specific external surface area compared to the non-oxidized counterpart. Consequently, it demonstrated superior MA (205.98 A g^{-1}_{catal}) and stability (maintaining nearly 100% activity for 48 h), outperforming commercial Pt/C (56.24 A g^{-1}_{catal}). This study highlights that oxidation-induced pore engineering is critical for optimizing the mass transport properties of ZIF-derived catalysts, paving the way for their application in high performance energy conversion technologies.

Received 5th November 2025,
Accepted 5th March 2026

DOI: 10.1039/d5nr04675k

rsc.li/nanoscale

1. Introduction

The oxygen reduction reaction (ORR) is a critical process in developing renewable energy storage and conversion technologies, including anion exchange membrane fuel cells (AEMFCs) and metal–air batteries.[1] Specifically, AEMFCs are distinguished by their high power density and rapid response capabilities, making them suitable for high-power applications. In contrast, metal–air batteries, such as Zn–air batteries, offer exceptionally high theoretical energy densities (*e.g.*, 1086 Wh kg^{-1} for Zn–air), far surpassing those of conventional lithium-ion batteries.[1] However, the slow kinetics and high overpotential associated with ORR pose significant obstacles to improving the power density of these energy applications.[2] Although Pt-based materials are well-known for their highly efficient ORR electrocatalytic properties, their high cost, limited availability, and poor durability hinder their large-scale commercial use.[3] Consequently, considerable efforts have focused on identifying cost-effective and abundant alternatives, particularly Pt-group-metal-free catalysts.[4–6] In particular, multicomponent catalysts composed of transition metals, N, and C (TM/N/C) have emerged as promising candidates because of their strong catalytic activity and low cost.[7] Despite extensive research on high-performance TM/N/C catalysts, most of these materials fail to achieve the ORR mass activity (MA) of commercial Pt/C catalysts. The TM/N/C catalysts required significantly higher loadings to match the performance of Pt/C.[8,9] However, this increased catalyst loading leads to a greater mass transfer resistance at high current densities, mainly because of the thicker catalyst layer. Therefore, further research is crucial for improving the MA of TM/N/C catalysts, with the ultimate goal of replacing commercial Pt-based catalysts.[10–12]

In general, the electrocatalytic MAs of TM/N/C catalysts are primarily influenced by two key factors: (i) the intrinsic catalytic activity and (ii) the number of active sites.[13] These factors are

[a]*Department of Organic and Nano Engineering, Human-Tech Convergence Program, Hanyang University, Seoul 04763, Republic of Korea. E-mail: than@hanyang.ac.kr*
[b]*Advanced Battery Research Center, Advanced Materials Division, Korea Research Institute of Chemical Technology, 141 Gajeong-ro, Yuseong-gu, Daejeon 34114, Republic of Korea*
[c]*Department of Chemical Engineering, Hanyang University, Seoul 04763, Republic of Korea. E-mail: yjang53@hanyang.ac.kr*
[d]*Department of Battery Engineering, Hanyang University, Seoul 04763, Republic of Korea*
† Equally contributed.

closely linked to the density of active sites and the efficiency of the mass transport of reactants to these sites. Furthermore, these can be improved through structural modifications, such as by optimizing the pore structure and morphology.[14] Recently, zeolitic imidazolate frameworks (ZIFs), a class of metal–organic frameworks (MOFs), have emerged as highly effective precursors for producing TM/N/C catalysts. Carbon materials derived from ZIFs offer the distinct advantage of retaining their original morphology and high specific surface area even after high-temperature carbonization.[15] Various catalyst designs have been developed using ZIF precursors through approaches such as transition metal exchange (*e.g.*, Co, Fe, and Cu), ligand exchange, guest molecule adsorption, introduction of additional compounds, and formation of core–shell structures.[16–21] However, notably, carbon materials derived from ZIFs typically exhibit a predominantly microporous structure owing to their intrinsic microporosity.[22–24] Additionally, the microstructure and sintering of metal nanoparticles during high-temperature pyrolysis often limit the exposure of catalytically active sites.[25,26] Consequently, there has been continued reliance on time-consuming and costly post-treatment processes, such as acid leaching and secondary annealing, to improve the mass transfer efficiency.[10–12]

Therefore, simple and effective methods must be urgently developed to expand the pore structure of ZIF-derived catalysts and achieve high ORR MA. In this study, we present a novel approach for preparing mesoporous electrocatalysts of Co, N, and C (Co/N/C) from ZIF precursors *via* the combined thermal oxidation of Co- and Zn-coordinated ZIFs (Zn, Co-ZIF). This process introduces O species that etch the catalyst surface during pyrolysis, enlarging the micropores and modifying the Zn, Co-ZIF morphology. The pore structure, specific surface area, and electrocatalytic MA of the resulting catalysts were strongly influenced by the oxidation conditions, particularly the oxidation temperatures of the Zn, Co-ZIF precursor. Notably, the catalyst oxidized at 310 °C and subsequently carbonized shows a 1.5-fold increase in its external surface area and a three-fold increase in its mesopore volume compared to the non-oxidized catalyst. Because the chemical compositions of all ZIF-based catalysts are similar, the observed differences in ORR MA can be primarily attributed to variations in their pore structures, which directly affect the mass transfer efficiency. We performed electrochemical impedance spectroscopy (EIS) to clarify the relationship between the mass transfer resistance and the effects of micropore enlargement due to oxidation pre-treatment. Consequently, the catalysts with the highest mesopore volume, induced by the oxidation pre-treatment, demonstrated the highest ORR MA and the lowest mass transfer resistance among other ZIF-based catalysts. Moreover, these catalysts outperform commercial Pt/C in alkaline media in terms of electrochemical performance.

2. Experimental

2.1. Materials

Cobalt(II) nitrate hexahydrate ($Co(NO_3)_2{\cdot}6H_2O$), zinc nitrate hexahydrate ($Zn(NO_3)_2{\cdot}6H_2O$), 2-methylimidazole (MeIM), DCD, commercial Pt/C (20 wt% Pt on Vulcan XC72), methanol, ethanol, and isopropanol were purchased from Sigma-Aldrich. Nafion® D-521 dispersion (5 wt%) was purchased from Alfa Aesar. All chemicals were used as received without further purification. Ultrapure deionized (DI) water was obtained using a Direct-Q3 system (Millipore Inc.) and used for all electrochemical experiments.

2.2. Synthesis of Zn, Co-ZIF

$Co(NO_3)_2{\cdot}6H_2O$ (2.16 mmol) and $Zn(NO_3)_2{\cdot}6H_2O$ (10.8 mmol) were dissolved in 200 mL of methanol, which was subsequently poured into 160 mL of methanol containing 54 mmol of 2-methyilimidazole. After vigorous stirring for 15 min, the solution was aged for 24 h at room temperature. The precipitate was centrifuged, washed with methanol several times to remove unreacted precursors, and dried at 60 °C in a vacuum oven overnight.

2.3. Synthesis of oxidized ZIF and Co/N–C series

The Zn, Co-ZIF powder was heat-treated at different temperatures (280, 310, and 340 °C) in a tube furnace with a heating rate of 2 °C min^{-1} in the air atmosphere for 2 h, producing O-ZIF@x, wherein x (x = 280, 310, 340) represents the oxidation temperature. Initially, 300 mg of O-ZIF@x was dispersed in ethanol (100 mL), and then 50 mL of ethanol containing 90 mg of DCD was added. After 3 h of stirring, the mixture was collected using a rotary evaporator. The obtained powder was carbonized at 900 °C (5 °C min^{-1}) in a tube furnace for 3 h under an Ar atmosphere, resulting in the Co/N–C_y (y = 1, 2, 3, and 4, which are derived from Zn, Co-ZIF, O-ZIF@280, O-ZIF@310, and O-ZIf@340, respectively). Carbonized ZIF obtained from non-oxidized Zn, Co-ZIF, was prepared using the same method as that used for the other samples.

2.4. Characterization

Thermogravimetric analysis (TGA) was performed using an SDT Q 600 instrument (TA instruments) between 25 and 800 °C at a heating rate of 5 °C min^{-1} in an air atmosphere. X-ray diffraction (XRD) patterns were examined on a MiniFlex60 operating at 30 kV and 20 mA with Cu Kα radiation λ = 1.5405 Å. Scanning electron microscopy (SEM) analysis was conducted using S4800 (Hitachi, Japan) at 15 kV and 10 μA with platinum sputtering at 20 mA for 10 s. High-angle annular dark field-scanning transmission electron microscopy (HAADF-STEM) images and Energy-dispersive X-ray spectroscopy (EDS) mapping images were captured on a NEOARM (JEOL) microscope with an accelerating voltage of 200 kV. X-ray photoelectron spectroscopy (XPS) was carried out using a theta-probe-based system (Al Kα radiation; Thermo Fisher Scientific) with an electron flood gun. Fourier-transform infrared (FT-IR) spectroscopy was performed on a Nicolet iS50 (Thermo Fisher Scientific) using the attenuated total reflectance (ATR) method. Solid-state ^{13}C NMR spectra were obtained using a 500 MHz Avance III HD Bruker solid-state nuclear magnetic resonance (NMR) spectrometer. The Brunauer–Emmett–Teller (BET) N_2 adsorption isotherm and

pore size distribution were obtained at 77 K using 3Flex (Micromeritics).

2.5. Electrochemical measurements

All electrochemical analyses were performed using a computer-controlled potentiostat (WaveDriver 200, Pine Research Instrumentation, USA, and VSP, Bio-Logic SAS instrument, France) with a three-electrode system equipped with a gas flow system. A glassy-carbon (GC) (5 mm diameter, 0.1963 cm^2 geometric surface area, Pine Research, USA), a Pt plate, and Hg/HgO served as the working, counter, and reference electrodes, respectively. The catalyst inks were prepared by ultrasonically dispersing 6 mg of the catalyst in a solution containing 0.94 mL of ethanol and 60 μL of a 5 wt% Nafion solution. The working electrodes were prepared by drop-casting 12.4 μL of the prepared sample suspensions (6 mg mL^{-1}) onto the surface of the GC electrode to achieve a catalyst loading of 0.379 mg cm^{-2}. For comparison, a commercial Pt/C (20 wt%) with a loading amount of 0.1 mg cm^{-2} was also electrochemically analyzed. The ORR performance was evaluated in an O_2-saturated alkaline electrolyte (0.1 M KOH) at 298 K. The background current, which was measured in an N_2-saturated alkaline electrolyte, was subtracted from the ORR current for electrical double-layer capacity current correction. The RDE and RRDE measurements were conducted at a scan rate of 5 mV s^{-1} with various rotation speeds (400, 625, 900, 1225, 1600, and 2025 RPM) at room temperature, whereas the potential of the Pt ring electrode was maintained at 1.2 V (*vs.* RHE). The electron transfer number (n) and kinetic current density (J_k) were derived from the Koutecky–Levich (K–L) equations (eqn (1) and (2)) at various electrode potentials:

$$\frac{1}{J} = \frac{1}{J_{kin}} + \frac{1}{J_{diff}} = \frac{1}{J_{kin}} + \frac{1}{B \cdot \sqrt{\omega}} \quad (1)$$

$$B = 0.620 \cdot n \cdot F \cdot {D_{O_2}}^{2/3} \cdot \nu^{-1/6} \cdot C_{O_2} \quad (2)$$

where J (mA cm^{-2}) is the measured current density, J_{kin} and J_{diff} are the kinetic current density and diffusion current density, respectively; ω (rad per s) is the rotating speed, F is the Faraday constant (96 485 C mol^{-1}), C_{O_2} is the bulk concentration of O (0.00126 mol L^{-1}), D_{O_2} is the diffusion coefficient of O in 0.1 M KOH (1.93×10^{-5} cm^2 s^{-1}), and ν is the kinetic viscosity (0.0109 cm^2 s^{-1}). The mass activity (MA) was strictly calculated based on the mass-transfer-corrected kinetic current density (J_k) to exclude macroscopic mass-transport limitations. The J_k values at 0.8 V *vs.* RHE were derived from the K–L equation:

$$J_{kin} = \frac{J \times J_{diff}}{J_{diff} - J} \quad (3)$$

For a highly precise and comprehensive evaluation, the MA was normalized in two distinct ways: to the total catalyst loading mass (MA_{catal}) and to the absolute mass of Co species determined by ICP-OES (MA_{metal}). The apparent turnover frequency (TOF, s^{-1}) was calculated based on the mass-transfer-corrected kinetic current (J_k) to evaluate the activity. The formula used is:

$$TOF = \frac{J_k \times 10^{-3}}{n \cdot F \cdot N_{site}} \quad (4)$$

where N_{site} is the total moles of Co atoms per geometric area, determined by ICP analysis. Due to the coexistence of Co–N_x and varying sizes of Co nanoparticles, determining the exact number of surface-exposed active sites is challenging. Thus, by assuming 100% utilization of all bulk Co atoms, the reported values represent a highly conservative apparent TOF. The formula used is:

$$N_{site} = \frac{L_{catal} \times W_{Co}}{MW_{Co}} \quad (5)$$

where L_{catal} is the total catalyst loading mass per geometric area on the glassy carbon electrode (g cm^{-2}), W_{Co} is the mass fraction of Co in the catalyst obtained from the ICP analysis, MW_{Co} is the atomic weight of Co (58.93 g mol^{-1}). The electron transfer number was calculated from the slope of the K–L plot. The hydrogen peroxide (H_2O_2) selectivity and electron transfer number were calculated from the RRDE measurements using eqn (6) and (7):

$$H_2O_2\,(\%) = 200 \times \frac{I_R/N}{|I_D| + I_R/N} \quad (6)$$

$$n = 4 \times \frac{|I_D|}{|I_D| + I_R/N} \quad (7)$$

where I_D is the disk current, I_R is the ring current, and N is the current-collection efficiency of the platinum ring (N = 0.37). EIS was performed by sweeping frequencies over the range 0.02 Hz–100 kHz, acquiring six points per decade with an AC amplitude of 5 mV using a single sine mode at various potentials ($V_{0.5}$, $V_{0.5}$ – 26 mV, $V_{0.5}$ – 52 mV, $V_{0.5}$ – 78 mV, $V_{0.5}$ – 104 mV (*vs.* RHE), where $V_{0.5}$ is the potential at which current density is 0.5 mA cm^{-2}). The ORR stability test in O_2-saturated 0.1 M KOH was evaluated by chronoamperometry at a potential of 0.6 V (*vs.* RHE).

3. Results and discussion

The catalyst synthesis begins with the organometallic reaction of Zn^{2+} and Co^{2+} ions with the 2-methylimidazole ligand,[15] forming typical dodecahedral-shaped ZIF nanocrystals coordinated with Zn and Co (Zn, Co-ZIF) (Scheme 1). This is followed by air-annealing, which induces oxidation and results in the formation of oxidized ZIF (O-ZIF). The pristine Zn, Co-ZIF and O-ZIF are then mixed with dicyandiamide (DCD) to promote nitrogen doping or the formation of nitrogen-containing species, followed by carbonization at high temperatures to produce cobalt-embedded nitrogen doped carbons (Co/N–Cs). The air-annealing temperature is determined based on the thermogravimetric analysis (TGA) of the as-prepared Zn, Co-ZIF, conducted while heating in air at a rate of 5 °C min^{-1}

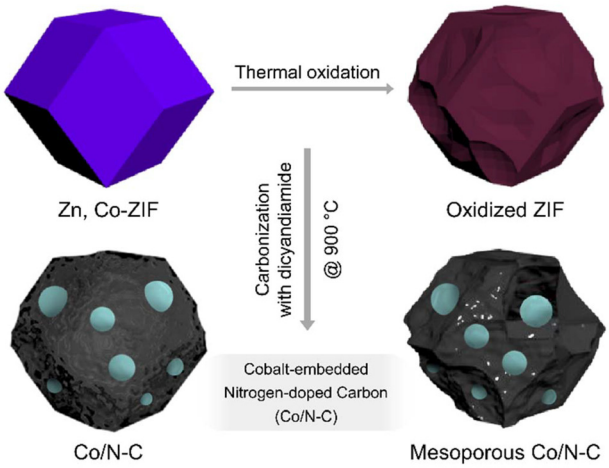

Scheme 1 Schematic illustration of the synthesis process of Co/N–C by direct carbonization of Zn, Co-ZIF and mesoporous Co/N–C by carbonization following additional thermal oxidation of Zn, Co-ZIF.

(Fig. S1). The decomposition process begins gradually at 270 °C, with significant weight loss occurring at approximately 370 °C. Notably, the extent of oxidation was highly dependent on both the time and temperature. However, TGA, which uses a continuously increasing temperature, does not fully capture the time-dependent nature of the oxidation reaction.[27] To ensure complete oxidation of Zn, Co-ZIF below 370 °C, oxidation is performed at 280, 310, and 340 °C for 2 h, with a heating rate of 2 °C min^{-1}, corresponding to O-ZIF@280, O-ZIF@310, and O-ZIF@340, respectively. The oxidation features are visualized in Fig. S2 showing a gradual darkening color gradient for each powder sample. The color change is due to structural distortion as supported by the subsequent analysis results.

The morphological changes in Zn, Co-ZIF induced by the oxidation treatment were visible in the transmission electron microscopy (TEM) and scanning electron microscopy (SEM) images (Fig. 1a–d and S3). During thermal oxidation, Zn, Co-ZIF gradually shrink and develop concave structures, with the degree of shrinkage and structural changes depending on the oxidation temperature. For O-ZIF@340, which was oxidized at the temperature at which ZIF began to decompose, the concave morphology and particle aggregation were more pronounced compared to those at lower temperature conditions. These morphological transformations were further supported by changes in the crystal structure, as confirmed by X-ray diffraction (XRD) analysis (Fig. S4a). The XRD patterns of all oxidized ZIF samples maintain a crystalline structure similar to the original material, but with shifts in peak positions toward higher 2θ values (Fig. 1e). This shift, along with peak broadening and reduced intensity, suggests the introduction of nonuniform lattice strain, shrinkage, and disruption of the ZIF framework due to thermal oxidation.[28] To obtain more detailed information about the lattice changes, we employed a Williamson–Hall plot to calculate the crystallite sizes and strains based on the peak broadening relative to the Bragg angle (Fig. 1f).[29] The plot follows the equation:

$$\beta \cos\theta = \varepsilon(4 \sin\theta) + \frac{0.9\lambda}{D}$$

where β represents the full width at half maximum (FWHM) in radians, after correcting for instrumental broadening using a Si reference powder, θ is the Bragg angle, λ is the X-ray wavelength, and ε denotes the lattice strain. The lattice strain induced by heat treatment is determined as the slope of the plot of $\beta\cos\theta$ against $4\sin\theta$. A positive strain value indicates that the lattice is under tensile stress, which corresponds to lattice expansion.

After thermal treatment, the lattice strain increased significantly because of framework deformation, the extent of which varied according to the treatment temperature. While O-ZIF@280 showed minimal changes in the XRD peaks and lattice strain compared to Zn, Co-ZIF, both O-ZIF@310 and O-ZIF@340 exhibited significant alterations in the peak shape, position, and intensity. These changes were particularly notable for O-ZIF@340, which oxidized at a temperature near the decomposition threshold observed by TGA. The TEM and SEM images further corroborated these observations, showing more significant morphological changes in O-ZIF@340 than in the other samples. Additionally, the lattice strain of O-ZIF@340 was approximately 40 times higher than that of the unoxidized Zn, Co-ZIF, indicating that oxidation at higher temperatures destabilized the structure and led to distinct deformation. The divergence between the decrease in the lattice constant and the increase in the tensile stress arises from the different thermal behaviors of the imidazole rings and Zn–N bonds under heat treatment.[30] The shrinkage of the framework was primarily due to changes in the flexible and saturated Zn–N bonds, which contracted during thermal treatment. In contrast, the aromatic rings in the imidazole ligands undergo expansion owing to heat, generating tensile stress in the lattice. Consequently, while the lattice constant decreases because of framework contraction, the overall lattice strain increases because of the expansion of the aromatic rings.

Building upon this structural deformation, we concurrently analyzed the porosity evolution to establish its correlation with the observed lattice strain (Fig. 1f and Fig. S6). As the lattice strain intensifies with increasing temperature, a proportional decrease in BET surface area is observed, dropping from 1740.3 to 514.16 $m^2\ g^{-1}$. This inverse relationship indicates that the accumulated lattice strain is closely associated with the reduction of the microporous framework, serving as a key indicator of the structural transition toward a hierarchical architecture. However, rather than mere degradation, this process drives the transition toward a hierarchical mesoporous network (Table S1). The moderate lattice strain at 310 °C perfectly merges the fractured micropores into open channels, achieving the maximum BJH mesopore surface area (394.25 $m^2\ g^{-1}$) and volume (1.22 $cm^3\ g^{-1}$). Conversely, the excessive strain in O-ZIF@340 triggers a severe macroscopic collapse, abruptly reducing all porosity metrics. Ultimately,

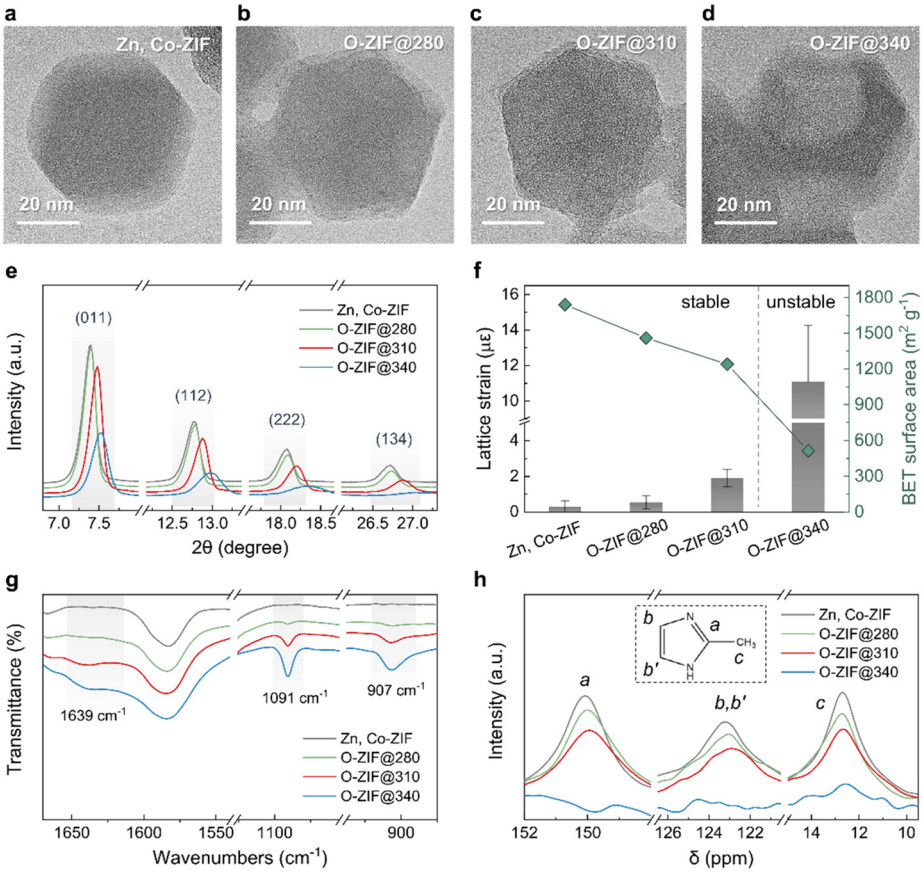

Fig. 1 Physical and chemical structure characterization of Co/N–Cs at various temperatures (0, 280, 310, 340 °C). (a–d) TEM images; (e) selected four XRD peaks; (f) lattice strain from Williamson–Hall plots and BET surface area; (g) enlarged view of FT-IR spectra corresponding to new peaks derived from heat treatment; (h) solid-state ^{13}C NMR spectra for oxidized ZIF series.

this optimally balanced defect-induced strain and maximized mesopore generation at 310 °C act as a robust structural template, laying the crucial foundation for the highly accessible hierarchical pore architecture in the final carbonized product.

Framework deformation was further confirmed by FT-IR spectroscopy (Fig. 1g and S4b). The heat-induced shrinkage of the framework introduces structural disorder in Zn, Co-ZIF. As the oxidation temperature increases, a shoulder develops on the higher wavenumber side of the peak at 1639 cm^{-1}, corresponding to C=C stretching vibrations. Additionally, new peaks appear at 1091 and 907 cm^{-1}, indicating the disordering of the molecular environment due to thermal oxidation, leading to weakened ring–ring interactions and changes in the electrical environment of the C–N bond.[30,31] The increasing intensities of these new FT-IR peaks correlate with the increasing lattice strain at higher oxidation temperatures. Moreover, the solid-state ^{13}C-NMR spectra of all oxidized ZIFs show upfield shifts in the peaks associated with the ring constituents (a and b, b′), indicating a disruption in the aromatic rings due to heat, consistent with the FT-IR observations. Meanwhile, the peaks corresponding to the methyl group (c) remained largely unchanged (Fig. 1h). In O-ZIF@340, the peaks corresponding to the carbons (a and b, b′) of the aromatic rings disappeared, likely due to an increase in bulk magnetic susceptibility caused by significant framework shrinkage,[32–37] which aligns with the observations from the lattice strain, TEM, and SEM images. At appropriate oxidation temperatures, Zn, Co-ZIF can effectively retain their intrinsic morphologies, demonstrating their high structural stability after heat treatment.[38] This suggests that the thermal oxidation pre-treatment can successfully modify the pore structure without significantly disrupting the overall morphology.

The chemical and elemental compositions of the oxidized ZIFs were investigated by XPS and FT-IR spectroscopy (Fig. 2). The increase in O content due to oxidation is evident in the high-resolution C 1s and O 1s spectra (Fig. 2a and b). A newly deconvoluted peak at a higher binding energy, corresponding to C–O bonds, gradually emerged for Zn, Co-ZIF and O-ZIF@340, reflecting the partial oxidation of the material. Additionally, the O 1s intensity, normalized to the C 1s intensity, increased, signifying the elevated presence of both physically and chemically adsorbed O species because of ligand oxidation.[39] The increase in the O/C ratio further confirmed the progressive introduction of O species at higher oxidation temperatures (Fig. 2c). Despite the noticeable changes in the C and O contents, the atomic ratios and chemical states of Zn, Co,

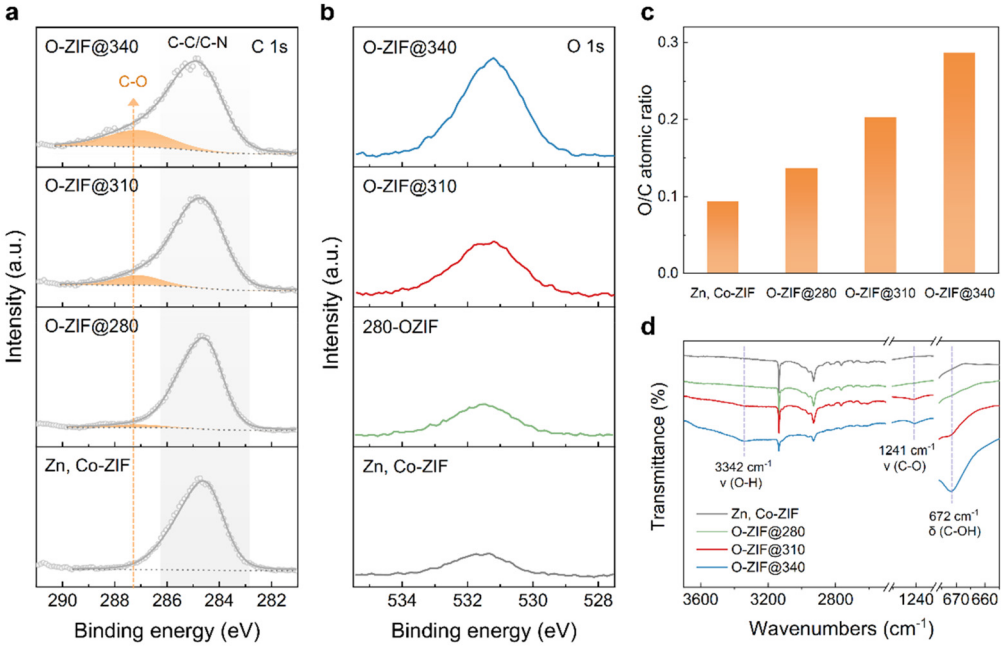

Fig. 2 Chemical composition characterization of oxidized ZIF. (a) XPS spectra of C 1s; (b) XPS spectra of O 1s normalized by the C1s intensity; (c) atomic ratio of O relative to C; (d) enlarged view of FT-IR spectra for the Co/N–C series.

and N in all the oxidized ZIFs remained stable (Table S2 and Fig. S5). This indicates that oxidation primarily affects C–O chemistry without significantly altering the metal or nitrogen species. The FT-IR spectra provided further evidence of an increase in chemisorbed hydroxyl groups due to oxidation (Fig. 2d and S4b). The broad absorption peak at 3342 cm^{-1} is attributed to O–H stretching vibrations, while the peaks at 1241 and 672 cm^{-1} correspond to C–O stretching and C–OH bending vibrations, respectively.[40] These adsorbed O species play a crucial role in the carbonization process by acting as pore-enlarging agents and contributing to the development of a mesoporous structure in the final catalyst.

The morphology and structural characteristics of the Co/N–Cs were analyzed using TEM (Fig. 3a–d). The obtained powder was carbonized at 900 °C (5 °C min^{-1}) in a tube furnace for 3 h under an Ar atmosphere, resulting in the formation of Co/N–C_*y* (*y* = 1, 2, 3, and 4, which are derived from Zn, Co-ZIF, O-ZIF@280, O-ZIF@310, and O-ZIf@340, respectively). Notably, Co/N–C_3 displayed an open hollow scaffold, which distinguished it from the Co/N–C_1 and Co/N–C_2 scaffolds. In contrast, Co/N–C_4 exhibited C particles entangled with carbon nanotubes (CNTs) and larger Co nanoparticles with an average diameter of approximately 15.02 nm. For comparison, Co/N–C_1, Co/N–C_2, and Co/N–C_3 had smaller mean diameters of approximately 10.17, 9.47, and 8.16 nm, respectively (Fig. S7). These observations suggest that the increased introduction of O species and more pronounced morphological deformation in Co/N–C_4 could lead to structural collapse, promoting Co sintering and catalyzing CNT growth during carbonization. The formation of these CNTs can be attributed to the *in situ* catalytic growth mechanism catalyzed by the metallic Co nanoparticles. During the high-temperature carbonization at 900 °C, the Co nanoparticles catalyze the decomposition of volatile carbon species generated from the ZIF organic linkers and DCD, leading to the nucleation and growth of CNTs on the Co surfaces.[16] Additionally, the XRD patterns of the Co/N–C samples revealed a (002) diffraction peak characteristic of graphitic carbon at approximately 26°, along with the presence of metallic Co (Fig. S8).[41] To verify the elemental distribution after carbonization, TEM-EDS mapping was performed on the optimized catalyst (Fig. S9). The images display a homogeneous distribution of C, N, O, and Co, confirming the successful incorporation of nitrogen and oxygen into the carbon framework. In particular, the Zn signal is barely detectable compared to the other elements. This stark contrast serves as direct evidence of the effective evaporation of Zn species during the 900 °C heat treatment, which is the key mechanism driving the formation of the mesoporous architecture. To further understand the effects of thermal oxidation on the micropore structure and surface area, N_2 adsorption–desorption isotherms were compared (Fig. 3e). The isotherms reveal clear differences in the porosity hysteresis loops of the catalysts with and without oxidation pre-treatment prior to carbonization. All samples exhibit type-IV isotherms, which are typically associated with mesoporous materials.[42,43] The Co/N–C_1 catalyst displays a type H3 hysteresis loop, indicating the retention of microporosity. Despite the release of corrosive gases from DCD and the evaporation of Zn during carbonization, which contributed to a more mesoporous structure in Co/N–C_1,[44] the intrinsic microporous nature of Zn, Co-ZIF remained, with micropores accounting for 29.4% of the total pore volume (Table 1). In contrast, the catalysts subjected to

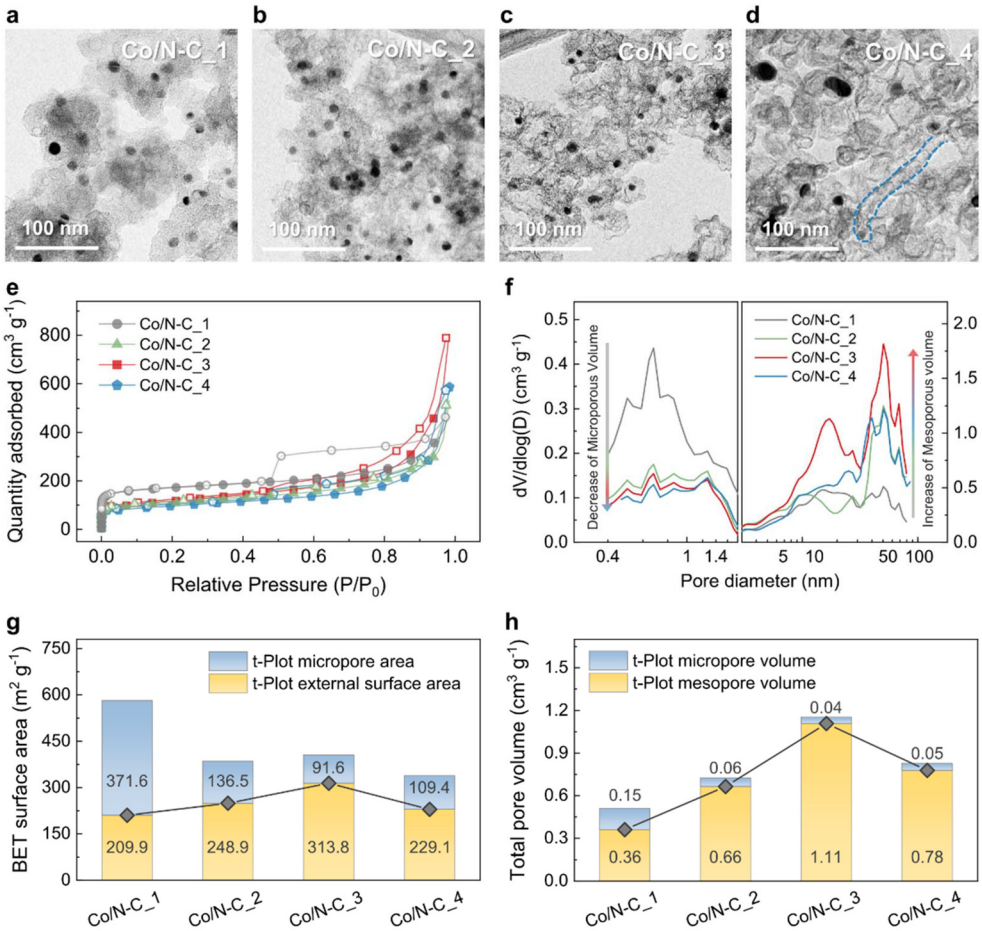

Fig. 3 Pore feature analysis for the Co/N–C series. (a–d) TEM images; (e) N_2 adsorption–desorption isotherms; (f) corresponding pore size distribution; (g) BET surface area; (h) total pore volume of Co/N–C_1, Co/N–C_2, Co/N–C_3, and Co/N–C_4.

Table 1 Pore volume and specific surface area derived from N_2-sorption isotherms of the Co/N–C series

	Pore volume ($cm^3\ g^{-1}$)			Specific surface area ($m^2\ g^{-1}$)		
Sample	V_{tot}	V_{micro}	V_{meso}	S_{BET}	S_{micro}	S_{ext}
Co/N–C_1	0.5165	0.1542 (29.4%)	0.3623	633.0	406.8	226.2
Co/N–C_2	0.7250	0.0605 (8.3%)	0.6645	385.5	136.5	248.9
Co/N–C_3	1.1531	0.0442 (3.8%)	1.1089	405.4	91.6	313.8
Co/N–C_4	0.8273	0.0494 (6.0%)	0.7779	338.6	109.4	229.2

the oxygen pre-treatment exhibited H4 hysteresis loops. As the oxidation temperature increased, the proportions of micropore volume in Co/N–C_2, Co/N–C_3, and Co/N–C_4 decreased significantly by 8.3%, 3.8%, and 6.0%, respectively (Table 1). These results provide compelling evidence for the effective pore-enlarging effect achieved through the thermal oxidation pre-treatment.

The pore volumes and specific surface areas of the catalysts are shown in Fig. 3g, h and Table 1. Following the thermal oxidation pre-treatment, the specific surface area of the carbonized catalysts decreased, while the specific external surface area increased, and the specific micropore area decreased. Additionally, the total pore volume increased with a concurrent reduction in the micropore volume and an increase in the mesopore volume. These results suggest that the micropores were transformed and enlarged into mesopores, likely due to surface etching effects from the introduced O species during the thermal oxidation pre-treatment of Zn, Co-ZIF before carbonization. This transformation is evident in the pore size distributions (Fig. 3f), where small micropores <1.8 nm, which limit participation in the ORR owing to accessibility issues, became relatively larger pores (above 2 nm) through thermal oxidation. The enlargement of micropores enhances the mass transport of reagents to the active sites, thus improving the ORR MA.[45] With increasing oxidation pre-treatment temperature (280 and 310 °C), the fraction of pores larger than 2 nm increased, confirming the conversion of micropores into mesopores. However, at a higher oxidation temperature (340 °C), pores in this size range decreased owing to structural collapse, the formation of larger Co nanoparticles, and the entangle-

ment of CNTs. Consequently, Co/N–C_3 exhibited the highest external surface area and mesopore volume among all the catalysts. These findings indicate that thermal oxidation pre-treatment at an optimal temperature effectively enlarges the intrinsic micropores of the ZIF structure into mesopores during carbonization, which is facilitated by the induced O functionalities.

XPS analysis was conducted to elucidate the chemical structures and the intrinsic nature of the active sites (Fig. S10). The high-resolution N 1s spectra were deconvoluted into pyridinic N (398.6 eV), pyrrolic N (400.5 eV), graphitic N (402.2 eV), and oxidized N (404.9 eV).[46] Normalizing these spectra at 398.6 eV revealed nearly identical profiles, confirming consistent nitrogen coordination environments across all ZIF-based catalysts.[47] For the Co 2p spectra, a more precise comparison was conducted by overlapping the enlarged Co 2p1/2 region (796.4 eV). This explicitly confirmed that the chemical speciation of Co (specifically the coexistence and proportion of atomically dispersed Co–N_x moieties and metallic Co nanoparticles) remains unchanged regardless of the pre-treatment. Additionally, the overlapped O 1s spectra exhibited uniform shapes, indicating that the specific types of oxygen functional groups integrated into the carbon matrix were also well-preserved after high-temperature carbonization. The quantitative surface elemental contents were highly comparable, with N and Co levels ranging from 10.38–13.25% and 1.50–2.04%, respectively (Fig. S10f). Consequently, these results decisively demonstrate that the oxidative pre-treatment does not alter the fundamental chemical identities or coordination environments of the active sites, indicating that the pre-treatment exclusively governs the physical pore architecture and the effective density of accessible active sites.

ICP-OES analysis (Table S3) was conducted to quantify the bulk metal contents, revealing substantial Co contents (8.83–13.06 wt%) and minor Zn residues (1.16–4.93 wt%). During high-temperature pyrolysis, the majority of the volatile Zn species evaporates to serve as an intrinsic porogen, facilitating pore development while spatially isolating the Co species to mitigate severe agglomeration. Although a small fraction of Zn remains trapped within the carbon matrix, these residual Zn^{2+} species possess a fully occupied closed-shell $3d^{10}$ electronic configuration. This intrinsic electronic state strictly hinders effective orbital hybridization and electron transfer with O_2, rendering the residual Zn fundamentally inert for oxygen-involved catalysis.[48] Consequently, this compositional analysis confirms that the heavily retained Co species function as the exclusive active centers within the synthesized porous architectures.

The increased external surface area and pore volume of the catalysts are expected to improve the ORR by reducing the mass transfer resistance. To verify this, catalytic ORR activities were measured using cyclic voltammetry (CV) (Fig. S11) and linear sweep voltammetry (LSV) with the RDE technique at different rotation speeds (400–2025 rpm) in 0.1 M KOH (Fig. S12). In the N_2-saturated electrolyte, the optimized Co/N–C catalyst exhibited the largest rectangular voltammetric loop compared to other control samples (Fig. S11e). This significant increase in the double-layer capacitance (C_{dl}) indicates a greatly enhanced electrochemically active surface area, attributed to the formation of a hierarchical porous structure derived from the evaporation of Zn species during the thermal activation process, which matched the BET results. Upon switching to the O_2-saturated electrolyte, distinct cathodic reduction peaks appeared for all samples (Fig. S11f). Notably, the Co/N–C_3 catalyst displayed the most positive peak potential and the highest peak current density. This superior ORR activity suggests that the optimized mesoporous architecture facilitates efficient mass transport of oxygen species to the abundant Co–N_x active sites. Following the qualitative assessment of ORR activity *via* CV, the reaction kinetics were further scrutinized using RDE measurements. As shown in the linear sweep voltammetry LSV curves, the current density increased linearly with the square root of the rotation speed, and the corresponding K–L plots exhibited good linearity and parallelism. This suggests that the ORR on the Co/N–C catalysts follows first-order reaction kinetics with respect to the concentration of dissolved oxygen (Fig. S12). For a clearer comparison, the LSV curves obtained at 1600 rpm are collectively presented in Fig. 4a. The diffusion-limited current densities of Co/N–C_1, Co/N–C_2, Co/N–C_3, and Co/N–C_4 were found to be 4.65, 5.06, 5.8, and 5.2 mA cm^{-2}, respectively. All ZIF-derived catalysts showed a similar trend in the onset potential, which was higher than that of commercial Pt/C. However, distinct differences were observed in the half-wave potentials (V *vs.* RHE at 3 mA cm^{-2}) (Fig. S13), suggesting that the mesoporous structure facilitates efficient mass transfer to the active sites.[16] Notably, the half-wave potential and limiting current density of Co/N–C_3 surpassed those of other ZIF-derived catalysts and outperformed commercial Pt/C. The Tafel slope of Co/N–C_3 (65.56 mV dec^{-1}) was significantly lower than those of the other ZIF-derived catalysts and Pt/C (86.24 mV dec^{-1}) (Fig. 4b), indicating superior MA. Additionally, the electron-transfer numbers (n) were calculated using rotating ring-disk electrode (RRDE) measurements at 1600 rpm, which confirmed that Co/N–C_3 followed a direct four-electron pathway for the ORR (n > 3.8) (Fig. S14 and S15a). This high selectivity suggests that the optimized catalyst effectively facilitates the direct four-electron pathway, thereby minimizing the production of corrosive peroxide intermediates that can degrade the catalyst and membrane. In a long-term stability test conducted at 0.6 V (*vs.* RHE), Co/N–C_3 retained nearly 100% of its activity after 48 h, whereas the commercial Pt/C retained only 30% after 24 h (Fig. S14b). This rapid decay in Pt/C is typically attributed to the agglomeration of Pt nanoparticles or carbon corrosion under alkaline conditions. Conversely, the robust stability of Co/N–C_3 implies that the Co active sites are strongly coordinated within the nitrogen-doped carbon matrix, preventing metal leaching and structural collapse during long-term cycling.

The ORR activity and stability of Co/N–C_3 were benchmarked against recently reported MOF-derived catalysts (Table S4). To ensure fairness, the performance was evaluated relative to commercial Pt/C. As shown in Table S4, Co/N–C_3

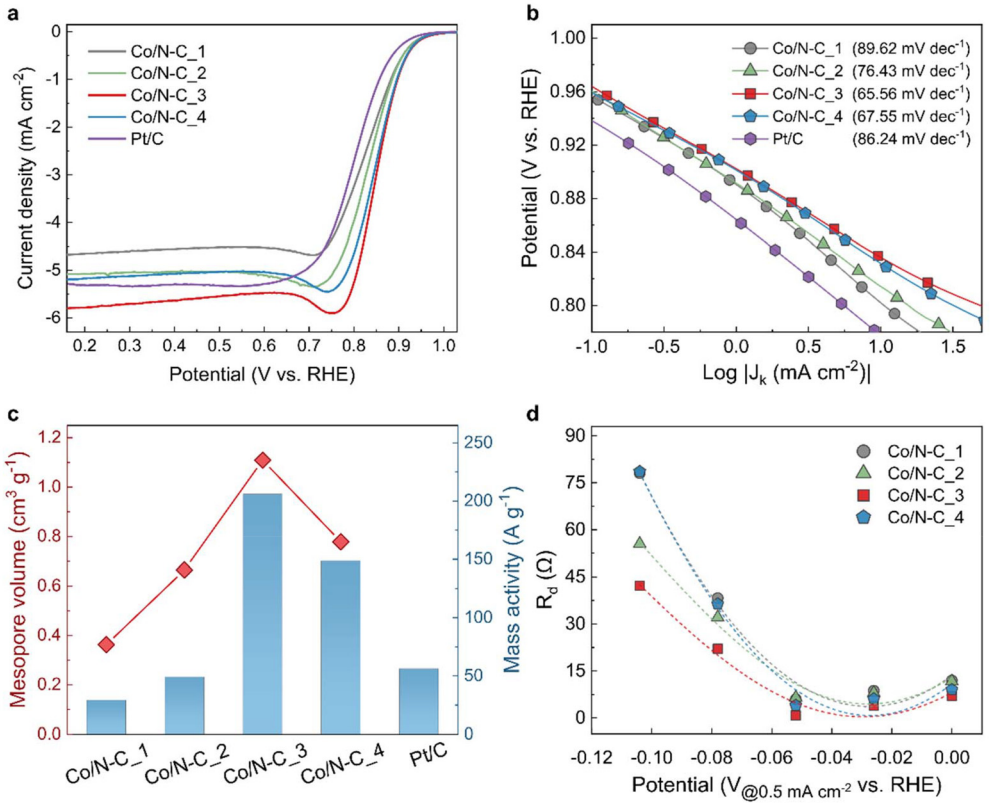

Fig. 4 Electrochemical analysis of the Co/N–Cs. (a) LSV polarization curves; (b) Tafel plot of Co/N–C_1, Co/N–C_2, Co/N–C_3, Co/NC_4, and Pt/C in O_2-saturated 0.1 M KOH at 1600 rpm, scan rate 5 mV s^{-1} (c) mesoporous volume of Co/N–C series and MA at 0.8 V (*vs.* RHE) of Co/N–C series and Pt/C. (d) Mass transfer resistance (R_d) calculated from impedance spectra at the different potentials of Co/NC series.

exhibits intrinsic activities ($\Delta E_{1/2}$) comparable to state-of-the-art catalysts reported between 2020 and 2025. Notably, its electrochemical stability stands out among the reported values; while many ZIF-derived catalysts show significant degradation within 24 h, Co/N–C_3 maintained negligible activity loss (~100% retention) over 48 h, demonstrating the robustness of the oxidation-derived mesoporous framework.

To provide a more quantitative assessment of the intrinsic electrocatalytic activity, we rigorously evaluated the MA and apparent TOF based on the mass-transfer-corrected kinetic current (J_k). All parameters used for these calculations are systematically summarized in Table S5. The correlation analysis reveals that the catalytic performance is directly proportional to the evolution of mesoporosity (Fig. 4c). Specifically, Co/N–C_3, which possesses the largest mesopore volume (1.11 cm^3 g^{-1}), achieved an exceptional catalyst-based MA of 205.98 A g^{-1}_{catal}. This value is not only substantially higher than those of other ZIF-derived counterparts but also significantly outperforms commercial Pt/C (56.24 A g^{-1}_{catal}). The apparent TOF was evaluated based on J_k and total bulk Co mass (Table S5) to isolate the catalytic performance from macroscopic mass-transport phenomena. While direct TOF comparisons in heterogeneous systems containing both Co–N_x and Co nanoparticles of varying sizes require careful interpretation, the apparent TOF provides a conservative yet valuable metric. Remarkably, the Co/N–C_3 catalyst exhibited an outstanding apparent TOF of 0.2409 s^{-1} (@0.8 V *vs.* RHE), substantially outperforming other Co/N–C samples and commercial Pt/C (0.1421 s^{-1}). Even factoring in the structural complexity, this clear trend substantiates that the mesoporous architecture significantly increases the effective density of accessible active sites, thereby maximizing the overall performance of the catalyst electrode.

To confirm that the mesoporous structure indeed improves mass transfer during ORR, we performed EIS on the ZIF-based catalysts at 1600 rpm across various potentials ($V_{0.5}$, $V_{0.5}$ – 26, $V_{0.5}$ – 52, $V_{0.5}$ – 78, $V_{0.5}$ – 104 mV *vs.* RHE, where $V_{0.5}$ represents the potential at which the current density is 0.5 mA cm^{-2}) (Fig. S16). The measured overall polarization resistance (R_p) was further analyzed by separating it into charge transfer and mass transfer resistances (R_{ct} and R_d).[49] In the initial potential range, where a high charge-transfer resistance is expected, all ZIF-based catalysts showed a decrease in the total electrochemical resistance (R_{ct} + R_d) as the potential decreased (from $V_{0.5}$ to $V_{0.5}$ – 52 mV) (Fig. S17). This behavior reflects the predominance of charge-transfer resistance in the mixed diffusion-controlled region. However, as the potential decreased further (from $V_{0.5}$ – 52 to $V_{0.5}$ – 104 mV) and entered the mass-transport region, where the mass transfer resistance became more influential, the electrochemical resistance increased (Fig. 4d, S17, and S18).

Consistent with the MA and mesopore volumes, the R_d values of the ZIF-based catalysts reflect the effects of the oxidation pre-treatment temperature. As the temperature is raised to 310 °C, the R_d values, along with the extent of R_d increase with decreasing potential, become less pronounced, resulting in high MAs due to the increased mesopore volume from micropore enlargement. In contrast to Co/N–C_3, the R_d values and their increase with decreasing potential increased once again at a higher oxidation temperature of 340 °C, correlating with a reduction in mesopore volume caused by structural collapse and the presence of entangled CNTs. These findings indicate that the mesopore volume in ZIF-derived catalysts is key to enhancing MA and reducing R_d. Thus, the increased mesoporosity achieved through this oxidation strategy improves access to active sites, resulting in higher ORR activity compared to commercial Pt/C.

Ultimately, due to the inherent complexity of the dual-site system and the interplay of multiple compounding factors, establishing a direct causal relationship through site-specific probing remains analytically challenging.[50,51] However, considering the intrinsic chemical uniformity confirmed across the catalyst series, the results of this study clearly demonstrate an intimate correlation between the MA and the tailored pore architecture. This strongly supports the conclusion that the structurally optimized mesoporous network fundamentally governs the electrocatalytic efficiency by successfully maximizing the effective density of accessible active sites.

4. Conclusions

We present a strategic thermal oxidation pre-treatment for enhancing the MA of the ZIF-derived catalyst for ORR. Unlike direct pyrolysis, this pre-treatment induces tailored lattice strain and structural defects of Zn, Co-ZIF, serving as a foundational stage to drive the evolution of a hierarchical mesoporous network during the subsequent carbonization. This structural transformation markedly increases mesopore volume and external surface area, minimizing mass-transfer resistance as confirmed by EIS across various potentials. The optimized Co/N–C_3 catalyst achieved an outstanding apparent TOF and mass activity (205.98 A g^{-1}_{catal}) that surpassed commercial Pt/C (56.24 A g^{-1}_{catal}), with exceptional stability over 48 hours. Crucially, we have proven that these superior kinetics are driven by the maximization of the effective density of accessible active sites through strain-driven pore engineering. This oxidation-based approach provides a versatile pathway for tailoring the pore architecture of MOF-derived catalysts, paving the way for high-performance electrocatalysts in advanced energy conversion systems.

Author contributions

Yu Joong Kim: conceptualization, methodology, validation, investigation, writing – original draft, writing – review & editing. Ki Hwan Koh: conceptualization, methodology, validation, investigation, writing – original draft, writing – review & editing. Hyeong Jun Kim: additional experiments, investigation, validation. Hyeonhoo Lee: validation, investigation. Sima Umrao: investigation, resources. Youn Jeong Jang: conceptualization, writing – review & editing, supervision. Tae Hee Han: conceptualization, writing – review & editing, supervision, project administration, funding acquisition. Yu Joong Kim and Ki Hwan Koh contributed equally to this work.

Conflicts of interest

There are no conflicts to declare.

Data availability

The data supporting this article have been included as part of the supplementary information (SI). Supplementary information is available. See DOI: https://doi.org/10.1039/d5nr04675k.

Acknowledgements

This work was supported by the National Research Foundation (RS-2022-NR068166 and RS-2023-00284346) of Korea. The XPS and XRD analysis of the prepared samples was performed at the Hanyang LINC Analytical Equipment Center (Seoul).

References

1 F. Jaouen, E. Proietti, M. Lefèvre, R. Chenitz, J.-P. Dodelet, G. Wu, H. T. Chung, C. M. Johnston and P. Zelenay, *Energy Environ. Sci.*, 2011, **4**, 114–130.
2 X. F. Lu, B. Y. Xia, S.-Q. Zang and X. W. Lou, *Angew. Chem., Int. Ed.*, 2020, **59**, 4634–4650.
3 K. Kodama, T. Nagai, A. Kuwaki, R. Jinnouchi and Y. Morimoto, *Nat. Nanotechnol.*, 2021, **16**, 140–147.
4 G. Wu, K. L. More, C. M. Johnston and P. Zelenay, *Science*, 2011, **332**, 443–447.
5 X. X. Wang, M. T. Swihart and G. Wu, *Nat. Catal.*, 2019, **2**, 578–589.
6 A. Mehmood, M. Gong, F. Jaouen, A. Roy, A. Zitolo, A. Khan, M.-T. Sougrati, M. Primbs, A. M. Bonastre, D. Fongalland, G. Drazic, P. Strasser and A. Kucernak, *Nat. Catal.*, 2022, **5**, 311–323.
7 D. S. Su and G. Sun, *Angew. Chem., Int. Ed.*, 2011, **50**, 11570–11572.
8 E. Proietti, F. Jaouen, M. Lefèvre, N. Larouche, J. Tian, J. Herranz and J. P. Dodelet, *Nat. Commun.*, 2011, **2**, 416.
9 S. Ma, G. A. Goenaga, A. V. Call and D.-J. Liu, *Chem. – Eur. J.*, 2011, **17**, 2063–2067.
10 I. S. Amiinu, X. Liu, Z. Pu, W. Li, Q. Li, J. Zhang, H. Tang, H. Zhang and S. Mu, *Adv. Funct. Mater.*, 2018, **28**, 1704638.

11 C. Liu, J. Wang, J. Li, J. Liu, C. Wang, X. Sun, J. Shen, W. Han and L. Wang, *J. Mater. Chem. A*, 2017, **5**, 1211–1220.
12 L. Lin, Q. Zhu and A.-W. Xu, *J. Am. Chem. Soc.*, 2014, **136**, 11027–11033.
13 I. E. L. Stephens, A. S. Bondarenko, U. Grønbjerg, J. Rossmeisl and I. Chorkendorff, *Energy Environ. Sci.*, 2012, **5**, 6744–6762.
14 G. A. Ferrero, K. Preuss, A. B. Fuertes, M. Sevilla and M.-M. Titirici, *J. Mater. Chem. A*, 2016, **4**, 2581–2589.
15 Z. Wang, X. Ke, K. Zhou, X. Xu, Y. Jin, H. Wang and M. Sui, *J. Mater. Chem. A*, 2021, **9**, 18515–18525.
16 Y. Li, P. Zhang, L. Wan, Y. Zheng, X. Qu, H. Zhang, Y. Wang, K. Zaghib, J. Yuan, S. Sun, Y. Wang, Z. Zhou and S. Sun, *Adv. Funct. Mater.*, 2021, **31**, 2009645.
17 Z. Liang, H. Guo, G. Zhou, K. Guo, B. Wang, H. Lei, W. Zhang, H. Zheng, U.-P. Apfel and R. Cao, *Angew. Chem., Int. Ed.*, 2021, **60**, 8472–8476.
18 X. Chen, N. Wang, K. Shen, Y. Xie, Y. Tan and Y. Li, *ACS Appl. Mater. Interfaces*, 2019, **11**, 25976–25985.
19 X. Xie, C. He, B. Li, Y. He, D. A. Cullen, E. C. Wegener, A. J. Kropf, U. Martinez, Y. Cheng, M. H. Engelhard, M. E. Bowden, M. Song, T. Lemmon, X. S. Li, Z. Nie, J. Liu, D. J. Myers, P. Zelenay, G. Wang, G. Wu, V. Ramani and Y. Shao, *Nat. Catal.*, 2020, **3**, 1044–1054.
20 H. Zhang, S. Hwang, M. Wang, Z. Feng, S. Karakalos, L. Luo, Z. Qiao, X. Xie, C. Wang, D. Su, Y. Shao and G. Wu, *J. Am. Chem. Soc.*, 2017, **139**, 14143–14149.
21 Y. Pan, K. Sun, S. Liu, X. Cao, K. Wu, W.-C. Cheong, Z. Chen, Y. Wang, Y. Li, Y. Liu, D. Wang, Q. Peng, C. Chen and Y. Li, *J. Am. Chem. Soc.*, 2018, **140**, 2610–2618.
22 Y. Qian, T. An, K. E. Birgersson, Z. Liu and D. Zhao, *Small*, 2018, **14**, 1704169.
23 M. Thomas, R. Illathvalappil, S. Kurungot, B. N. Nair, A. A. P. Mohamed, G. M. Anilkumar, T. Yamaguchi and U. S. Hareesh, *ACS Appl. Mater. Interfaces*, 2016, **8**, 29373–29382.
24 Z. Liu, D. Ye, X. Zhu, S. Wang, Y. Zou, L. Lan, R. Chen, Y. Yang and Q. Liao, *Chem. Eng. J.*, 2022, **432**, 134192.
25 X. Li, C. Zeng, J. Jiang and L. Ai, *J. Mater. Chem. A*, 2016, **4**, 7476–7482.
26 J. Yang, H.-Q. Chen, N. Shi, T. Wang, J. Liu and W.-P. Pan, *Chem. Eng. J.*, 2022, **428**, 132095.
27 B. You, N. Jiang, M. Sheng, W. S. Drisdell, J. Yano and Y. Sun, *ACS Catal.*, 2015, **5**, 7068–7076.
28 H. Yin, H. Kim, J. Choi and A. C. K. Yip, *Chem. Eng. J.*, 2015, **278**, 293–300.
29 J. A. Thompson, K. W. Chapman, W. J. Koros, C. W. Jones and S. Nair, *Microporous Mesoporous Mater.*, 2012, **158**, 292–299.
30 V. Mote, Y. Purushotham and B. Dole, *J. Theor. Appl. Phys.*, 2012, **6**, 1–8.
31 K. S. W. Sing, D. H. Everett, R. A. W. Haul, L. Moscou, R. A. Pierotti, J. Rouquerol and T. Siemieniewska, *Pure Appl. Chem.*, 1985, **57**, 603–619.
32 C. Schlumberger and M. Thommes, *Adv. Mater. Interfaces*, 2021, **8**, 2002181.
33 W. Wu, W. Zhang, Y. Long, J. Qin and J. Ma, *Microporous Mesoporous Mater.*, 2021, **328**, 111472.
34 T. J. Bandosz, *Carbon*, 2022, **188**, 289–304.
35 R. K. Singh, R. Devivaraprasad, T. Kar, A. Chakraborty and M. Neergat, *J. Electrochem. Soc.*, 2015, **162**, F489–F498.
36 C. Wu, D. Xie, Y. Mei, Z. Xiu, K. M. Poduska, D. Li, B. Xu and D. Sun, *Phys. Chem. Chem. Phys.*, 2019, **21**, 17571–17577.
37 S. Gadipelli, W. Travis, W. Zhou and Z. Guo, *Energy Environ. Sci.*, 2014, **7**, 2232–2238.
38 A. A. Valeeva, S. Z. Nazarova and A. A. Rempel, *Phys. Status Solidi B*, 2016, **253**, 392–396.
39 L. Peng, R. J. Clément, M. Lin and Y. Yang, in *NMR and MRI of Electrochemical Energy Storage Materials and Devices*, ed. Y. Yang, R. Fu and H. Huo, The Royal Society of Chemistry, 2021, pp. 1–70.
40 A. V. Kuttatheyil, D. Lässig, J. Lincke, M. Kobalz, M. Baias, K. König, J. Hofmann, H. Krautscheid, C. J. Pickard, J. Haase and M. Bertmer, *Inorg. Chem.*, 2013, **52**, 4431–4442.
41 Y. A. Pankratova, Y. V. Nelyubina, V. V. Novikov and A. A. Pavlov, *Russ. J. Coord. Chem.*, 2021, **47**, 10–16.
42 R. Knorr, H. Hauer, A. Weiss, H. Polzer, F. Ruf, P. Löw, P. Dvortsák and P. Böhrer, *Inorg. Chem.*, 2007, **46**, 8379–8390.
43 J. Novotný, L. Jeremias, P. Nimax, S. Komorovsky, I. Heinmaa and R. Marek, *Inorg. Chem.*, 2021, **60**, 9368–9377.
44 K. S. Park, Z. Ni, A. P. Côté, J. Y. Choi, R. Huang, F. J. Uribe-Romo, H. K. Chae, M. O'Keeffe and O. M. Yaghi, *Proc. Natl. Acad. Sci. U. S. A.*, 2006, **103**, 10186–10191.
45 L. Tao, C.-Y. Lin, S. Dou, S. Feng, D. Chen, D. Liu, J. Huo, Z. Xia and S. Wang, *Nano Energy*, 2017, **41**, 417–425.
46 R. M. Salim, J. Asik and M. S. Sarjadi, *Wood Sci. Technol.*, 2021, **55**, 259–313.
47 H. S. Kim, C. H. Lee, J.-H. Jang, M. S. Kang, H. Jin, K.-S. Lee, S. U. Lee, S. J. Yoo and W. C. Yoo, *J. Mater. Chem. A*, 2021, **9**, 4297–4309.
48 Z. Yang, Y. Kong and C. Qi, *Nanoscale*, 2025, **17**, 1069.
49 J. F. Watts and J. Wolstenholme, *An Introduction to Surface Analysis by XPS and AES*, John Wiley & Sons Inc., 2019.
50 Y. Wu, Z. Wei, W. Wei and L. Sun, *ACS Sustainable Chem. Eng.*, 2025, **13**, 17003–17013.
51 D. Lyu, Y. Du, S. Huang, B. Y. Mollamahale, X. Zhang, S. W. Hasan, F. Yu, S. Wang, Z. Q. Tian and P. K. Shen, *ACS Appl. Mater. Interfaces*, 2019, **11**, 39809–39819.